EFFECTS OF MAGNETIC ANISOTROPY
AND EXCHANGE IN Tm_2Fe_{17}

A. N. Pirogov ^{a,c*}, *S. G. Bogdanov* ^{a}, *E. V. Rosenfeld* ^{a}, *J.-G. Park* ^{b},

Y. N. Choi ^{c}, *S. Lee* ^{c}, *K. Prokeš* ^{d}, *N. O. Golosova* ^{e}, *I. L. Sashin* ^{e},

N. V. Kudrevatykh ^{f}, *Yu. N. Skryabin* ^{a}, *A. P. Vokhmyanin* ^{a}

^{a} *Institute of Metal Physics, Ural Division, Russian Academy of Sciences*
620990, Ekaterinburg, Russia

^{b} *FPRD, Department of Physics and Astronomy, Seoul National University*
151-742, Seoul, Korea

^{c} *Neutron Science Division HANARO, Korea Atomic Energy Research Institute*
305-600, Daejeon, Korea

^{d} *Helmholtz Centre Berlin for Materials and Energy*
D-14109, Berlin, Germany

^{e} *Joint Institute for Nuclear Research*
141980, Dubna, Russia

^{f} *Institute of Physics and Applied Mathematics, Ural Federal University*
620083, Ekaterinburg, Russia

Neutron diffraction experiments have been carried out to study the magnetocrystalline anisotropy of two ($2b$ and $2d$) Tm sublattices and four ($4f$, $6g$, $12j$, and $12k$) Fe sublattices in ferrimagnetic compound Tm_2Fe_{17} (space group $P6_3/mmc$). We determine the temperature dependence of the magnitude and orientation of magnetization for each of the thulium and iron sublattices in the range (10–300) K. A spontaneous rotation (at about 90 K) of the Tm and Fe sublattice magnetizations from the c-axis to the basal plane is accompanied by a drastic change in the magnetization magnitude, signifying a large magnetization anisotropy. Both Tm sublattices exhibit an easy-axis type of the magnetocrystalline anisotropy. The Fe sublattices manifest both the uniaxial and planar anisotropy types. The sublattice formed by Fe atoms at the $4f$ position reveals the largest planar anisotropy constant. The Fe atoms at the $12j$ position show a uniaxial anisotropy. We find that the inelastic neutron scattering spectra measured below and above the spin-reorientation transition are remarkably different.

1. INTRODUCTION

Since the 1970s, compounds that comprise rare earth (R) and $3d$ transition (T) metals and exhibit large magnetocrystalline anisotropy (MA) and high Curie temperatures (T_C) have been the subject of intense investigations in view of possible engineering applications [1]. In general, the origin of such a beneficial combination of the properties just in the R–T compounds is quite clear. A strong exchange interaction in the T subsystem provides a high T_C, and the large MA mainly originates from the R ions. The orbital momentum of f-shell electrons is not quenched and its rotation in the crystalline electric field (CEF) of uniaxial symmetry results in a significant energy change.

However, quantitative calculations and predictions of the magnetic properties of R–T compounds are currently rather limited in their capacity. Even the sim-

*E-mail: pirogov05@gmail.com

plest phenomenological expression cannot be used directly to describe the energy of these compounds:

$$E = E_{an} - (\mathbf{H} \cdot \mathbf{M}),$$
$$E_{an} = K_1 \cos^2 \theta + K_2 \cos^4 \theta + \dots , \qquad (1)$$

where E_{an} is the MA energy, $\mathbf{H}$ is the external field, $\mathbf{M}(\theta, \phi)$ is the magnetization of a crystal, θ and ϕ are the polar and azimuthal angles of magnetization, and K_1 and K_2 are the first and the second MA constants. Equation (1) describes the case of uniaxial symmetry. The MA constants are chosen such that the dependences $\mathbf{M}(\mathbf{H})$ obtained from the minimization in Eq. (1) are fitted to experimental magnetization curves in the best way.

The problems emerging in such a procedure are partially caused by the dependence of the magnetization magnitude on θ, which is called the magnetization anisotropy effect. In some R–T compounds, the effect can reach tens of percent [2]. There is also a difficulty in the cases where higher-order constants K_2, K_3,... are comparable with or even larger than K_1.

To properly describe these and other peculiarities of the R–T compounds, it is necessary to use more realistic models, where main interactions responsible for the magnetic properties of the system are taken into account explicitly. Presently, models of the magnetic structure for R–T compounds are mainly based on the following assumptions.

First, in compounds with T = Co, Fe, the exchange interaction in the T subsystem is very strong ($T_C \approx \approx 1000$ K). Therefore, magnetization of the T subsystem ($\mathbf{M}_T$) can be regarded as a classical vector and the energy of this subsystem can be described by an expression of the type of Eq. (1). The first constant K_T is sufficient to describe the MA of the T subsystem. As a result, the energy of the T subsystem is given by

$$E_T = K_T \cos^2 \theta_T - H M_T \cos(\theta_T - \vartheta_H), \qquad (2)$$

where θ_T and ϑ_H are the respective angles formed by $\mathbf{M}_T$ and $\mathbf{H}$ with the c-axis.

Second, the exchange interaction in the R subsystem is usually rather weak (a typical temperature is about 30 K), and it is mostly neglected. In the R subsystem, the interaction of the electric quadrupole moment of the f-shell electrons with the CEF plays the main role (see, e.g., [3]). The Hamiltonian of this interaction is usually given in the form

$$H_{CEF} = B_{20} O_{20} + B_{40} O_{40} + \dots , \qquad (3)$$

where B_{nm} are the so-called CEF parameters and O_{nm} are the Stevens equivalent operators [4]. Formally,

varying the parameters B_{nm} allows changing the MA energy of the R subsystem in a wide range. But from the physical standpoint, the B_{nm} parameters are the coefficients in the expansion of the electric field of the crystal in Legendre polynomials, and it is therefore necessary to have in view what combination of B_{nm} corresponds to a specific charge-density distribution.

Third, in the R–T compounds, the exchange interaction between the R and T subsystems (called the intersublattice interaction) is extremely important because it magnetizes the R ions. The intersublattice interaction can be written in various ways. We write it as

$$H_{ex} = -I_{RT}(\mathbf{m} \cdot \mathbf{J}), \qquad (4)$$

where I_{RT} is the parameter of the R–T interaction, $\mathbf{J}$ is the operator of the total momentum of the R ion, and $\mathbf{m}$ is the unit vector in the direction of the T-spin moments. Assuming that the De Gennes rule holds for the isostructural R–T compounds, I_{RT} can be defined as

$$I_{RT} = (g_J - 1)I, \qquad (5)$$

where g_J is the Landé factor of the R ion with the momentum J and I is the exchange parameter, which is constant over a given series of compounds. Using Eqs. (2)–(5), we can write the energy of an R–T compound as

$$E = E_R + E_T,$$
$$E_R = -T \ln Z, \quad Z = \mathrm{Tr} \left\{ \exp \left(-\frac{H_R}{T} \right) \right\}, \qquad (6)$$
$$H_R = H_{CEF} + H_{ex} - g_J \mu_B (\mathbf{H} \cdot \mathbf{J}).$$

The energy E turns to be a function of several parameters: M_T, K_T, I, B_{20}, B_{40},... even in the case of the simplest R–T compound (with one R and one T sublattice). For such a magnet, the values of M_T and K_T are strongly limited and determined quite well from the experiments on isostructural Y–T (or Lu–T) compounds. The magnitudes of the CEF parameters and the intersublattice exchange (and, perhaps, the coupling in the R sublattice) have to be determined from the comparison of and consistency between the results of the largest possible number of various experiments. Quite suitable for that purpose are the R–T compounds with a spontaneous spin-reorientation transition (SRT) [5]. The SRT originates from a competition between the R- and T-subsystem anisotropies. The former dominates at lower temperatures, whereas the latter is dominant at higher temperatures. Many

different ways of finding the exchange and CEF parameters have evolved from the consideration of the SRT [6], because the relation between I, K_{T}, and B_{20} governs the temperatures of the beginning (T_{SR1}) and end (T_{SR2}) of the SRT, and the ratio between I and B_{20} determines the magnetization anisotropy in the R subsystem ($\Delta M_{\mathrm{R}} = M_{\mathrm{R}}(T_{SR1}) - M_{\mathrm{R}}(T_{SR2})$), and so on. The SRT may also be accompanied by a large magnetization anisotropy in the T subsystem [7]. It is also worth noting that an approximate compensation of the major anisotropic contributions of the R and T subsystems occurs in the SRT region, and that is why minor contributions (which are not seen at the background of anisotropic contributions) can be revealed there.

In this respect, the compound Tm_2Fe_{17} is a very suitable object, in which the SRT occurs at 90 K [8]. The Tm_2Fe_{17} compound has a potential of being applicable for studying the CEF. There are two ($2b$ and $2d$) types of Tm positions (Tm_b and Tm_d) even in the case of an ideal crystal structure. The nearest-neighbor Fe-atom surroundings of these sites are almost identical, whereas the thulium surroundings are quite different. Therefore, the CEFs that act on the Tm_b and Tm_d ions can be different; for example, it is reported in Ref. [9] that the parameters B_{20}^b and B_{20}^d (for Tm_b and Tm_d respectively) have different signs. Such a situation is of interest with regard to modern calculation techniques of the CEF [10, 11].

In Tm_2Fe_{17}, the Fe atoms also occupy diverse sites. No less than four Fe sublattices (Fe_f, Fe_g, Fe_j, and Fe_k) can be distinguished [12]. Their contributions to the MA energy of the Fe subsystem can also be different. It is hardly possible to determine the magnitudes and signs of these contributions if only the magnetization curves are measured. However, if the orbital momentum of the T atoms is incompletely quenched, this becomes possible by means of the neutron-diffraction data and the simplest phenomenological theory [13], as is described in what follows.

In this paper, we report an elastic and inelastic neutron scattering study on powder and single-crystal Tm_2Fe_{17}. This study was aimed at

1) determining the temperature dependences of magnetization for each of the two Tm and the four Fe sublattices;

2) studying the SRT and the magnetization anisotropy effect in the Tm and Fe sublattices;

3) determining the I, B_{20}^b, and B_{20}^d parameters and the MA constants of the Tm sublattices;

4) estimating the MA constants of the Fe sublattices.

2. EXPERIMENTAL DETAILS

The Tm_2Fe_{17} alloy was prepared by melting Tm (3N) and Fe (4N) elements in an induction furnace under a protective helium atmosphere. An excess of two at.% of thulium was used to compensate for the Tm evaporation. The powder sample was prepared by a pounding of the ingot. The single crystalline sample was grown by remelting the ingot in a tube furnace with a high temperature gradient and cooling slowly through the melting and the peritectic reaction temperature points. It was shaped as a spherule about 2 mm in diameter.

Rocking curves (ω-scans) of the single crystal were measured with the double-axis E-4 diffractometer at the Helmholtz Centre for Materials and Energy, Berlin, with the incident neutron wavelength 2.44 Å.

Neutron powder diffraction patterns were recorded with the HRPD diffractometer at the Neutron Science Division HANARO in the temperature region 10–300 K with the incident neutron length 1.835 Å. The scans were obtained in the range $2\theta = 7°$–$159°$ with a step of $0.05°$. In addition, a position-sensitive detector system was used for the measurements in the range $2\theta = 2°$–$6.7°$. The data analysis was done using the FULLPROF refinement package [14].

The inelastic neutron scattering (INS) experiment was carried out with KDSOG time-of-flight spectrometer with the inverse geometry at the pulsed reactor IBR-2 of the JINR. The spectra were measured at 10, 60, 120, and 300 K. Peculiarities of the KDSOG spectrometer (a Be filter before the detector and low energy resolution in the small energy transfer range) do not allow measurements in the energy range 0–2 meV. For these reasons, we performed the INS measurements in the energy transfer range 2–100 meV.

3. MODEL

As mentioned above, the exchange interaction in the R subsystem is very weak and, on the contrary, the exchange in the T subsystem is very strong. Then the spin momentum of the T subsystem ($\mathbf{M}_{\mathrm{T}}^S$) can be considered a classical vector, whose magnitude (and therefore the value of the I parameter in Eqs. (4) and (5)) depends only on temperature ($I \sim M_{\mathrm{T}}^S$). Both the exchange field from the T subsysten and the external field affect the R ion. The direction of $\mathbf{M}_{\mathrm{T}}^S$ entirely controls the E energy of a crystal, whose equilibrium corresponds to the minimum $E(\theta)$. At this equilibrium, the R-ion magnetic moment is determined from the equation

$$\mathbf{M}_R(\theta) = \frac{1}{Z} \operatorname{Tr}\left\{ \mathbf{J} \exp\left(-\frac{H_R(\theta)}{T}\right) \right\}. \qquad (7)$$

In applying this model to the Tm_2Fe_{17} compound, we take the presence of two Tm sublattices into account; then Eq. (6) for the energy should be rewrittten as

$$E = E_{Tm}^b(\theta, \mathbf{H}) + E_{Tm}^d(\theta, \mathbf{H}) +$$
$$+ K_{Fe}\cos^2(\theta) - (\mathbf{H}\cdot\mathbf{M}_{Fe}), \quad (8)$$

where E_{Tm}^b and E_{Tm}^d are the respective free energies of the $2b$ and $2d$ Tm sublattices and $\mathbf{M}_{Fe}$ is the magnetization of the Fe sybsystem.

In order to deal with a minimal number of fitting parameters, we assume that only the B_{20}^b and B_{20}^d parameters are not equal to zero in the case of Tm_2Fe_{17}. We assume the parameters I to be the same for both Tm sublattices, because they have almost identical Fe-neighbor surroundings. Hence, there are only three fitting parameters: I, B_{20}^b, and B_{20}^d. The temperature dependence of the I parameter is determined by $M_{Fe}(T)$, and it can be obtained from the neutron diffraction experiment. The value of K_{Fe} can be taken from the magnetic measurement data on the isostructural compounds, where R is nonmagnetic. We assumed $K_{Fe} = -3.1$ MJ/m^3 (or -58 K/f.u.) in our calculations as K_1 in Y_2Fe_{17} [16, 17].

The computation task amounts to determining the θ value that realizes the energy minimum at various temperatures, and to calculating the mean values of magnetizations $\mathbf{M}_{Tm}^b$ and $\mathbf{M}_{Tm}^d$ using Eqs. (7) and (8). As a result, we obtain the calculated temperature dependences of the orientations and magnitudes of the Tm_b and Tm_d sublattice magnetizations, which have to be fitted to experimental ones.

In addition to B_{20}^b and B_{20}^d, the MA constants of the Fe sublattices in Tm_2Fe_{17} can be estimated. Presently, it is believed that the large MA energy of the T subsystem originates from a large change in the orbital moment when the crystal magnetization rotates from the easy direction to the hard one [13, 18, 19]. We apply the model of the MA of a system with an incompletely quenched orbital magnetic moment, developed in Ref. [13]. The magnetic moment $\boldsymbol{\mu}_{Fe}$ of a Fe atom is the sum of contributions arising from the spin and orbital moments ($\mathbf{S}$ and $\mathbf{L}$, respectively). We assume that the S magnitude does not depend on the site occupied by the Fe atoms. The L value cannot be equal for different crystallographic positions because the quenching degree of the orbital moment depends on the local environment [12]. In accordance with Ref. [13], the MA energy of the Fe atom in Tm_2Fe_{17} can be expressed as

$$E_{an}^{Fe} = -\lambda\mathbf{L}\cdot\mathbf{S} + r_\parallel L_\parallel^2 + r_\perp L_\perp^2, \qquad (9)$$

where λ is the parameter of spin–orbital coupling, r is the coefficient of the quenching hardness, and "$\parallel$" and "$\perp$" subscripts denote the projection on the c-axis and on the basal plane. The equilibrium values of $L_\parallel$ and $L_\perp$ are obtained by minimizing the E_{An}^{Fe} energy:

$$L_\parallel = \frac{\lambda S}{2}r_\parallel\cos\theta, \quad L_\perp = \frac{\lambda S}{2}r_\perp\sin\theta. \qquad (10)$$

If we neglect changes of S with temperature over the SRT region, then the difference between $L_\parallel$ and $L_\perp$ gives rise to the Fe-atom magnetization anisotropy:

$$\Delta\mu_{Fe} = \mu_B\left[L_\perp\left(\theta = \frac{\pi}{2}\right) - L_\parallel(\theta = 0)\right] =$$
$$= \mu_B\lambda S\frac{r_\parallel - r_\perp}{2r_\parallel r_\perp}. \quad (11)$$

Expression (12) can then be rewritten as

$$E_{an}^{Fe} = -\frac{\lambda S^2}{4r_\parallel} - \frac{\lambda S\Delta\mu_{Fe}}{2\mu_B}\sin^2\theta. \qquad (12)$$

Therefore, the MA constant of the νth Fe sublattice in Tm_2Fe_{17} is

$$K_{Fe}^\nu = -\frac{\lambda S}{2\mu_B}\Delta\mu_{Fe}^\nu. \qquad (13)$$

Assuming that λ is the same for all Fe atoms, we can write the proportion

$$K_{Fe}^f : K_{Fe}^g : \ldots : K_{Fe} =$$
$$= \Delta\mu_{Fe}^f : \Delta\mu_{Fe}^g : \ldots : \Delta\mu_{Fe}, \quad (14)$$

where f and g are the letters of Wyckoff positions occupied by the Fe atoms. We also assume that K_{Fe} is the sum of the MA constants of the Fe sublattices:

$$n^f K_{Fe}^f + n^g K_{Fe}^g + \ldots = K_{Fe}, \qquad (15)$$

where n^f and n^g are the occupation numbers of the f- and g-positions. System of Eqs. (14) and (15) allows estimating the MA constant of each of the Fe sublattices if the value of K_{Fe}, the occupation numbers, and the magnetization anisotropy for the different Fe-atom positions are known.

4. RESULTS AND ANALYSIS

The evolution of the neutron powder diffraction patterns of Tm_2Fe_{17} between 10 and 300 K is shown in Fig. 1. A refinement of the 288 and 300 K patterns,

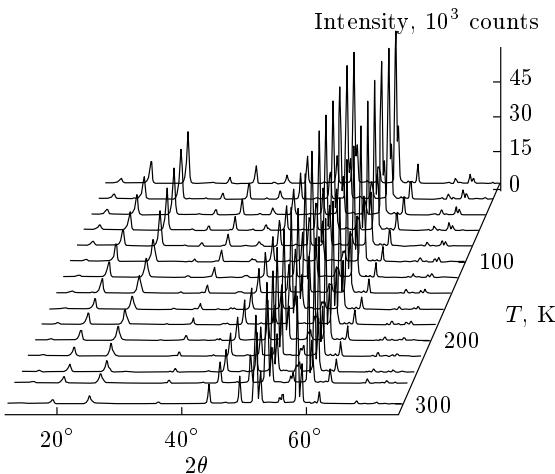**Fig. 1.** Neutron diffraction patterns of $Tm_{1.83}Fe_{17.34}$ in the temperature range 10–300 K. Curves are moved for clarity. The first half of the angle interval of patterns is shown

Fig. 2. Evolution of the magnetic scattering with temperature in the small-angle part of the neutron diffraction patterns, measured at (*a*) 281 K, (*b*) 266 K, (*c*) 257 K, and (*d*) 238 K

collected in the paramagnetic state, has shown that the sample contains a small amount (about 4 %) of the Tm_2O_3 impurity phase. The reflections of this phase partly overlap the ones of the main phase. The disordered model of the Th_2Ni_{17}-type structure (space group $P6_3/mmc$) proposed in Ref. [20] was used in the course of our refinements. The obtained values of the lattice and coordinate parameters are presented in Table 1. The occupation numbers are as follows: for the Tm ions, $n = 0.78(1)$, $1(0)$, and $0.05(2)$ respectively at the $2b$, $2d$, and $2c$ positions; for the Fe atoms, $n = 0.95(2)$, $0.22(1)$, $1(0)$, $0.64(2)$, $0.36(2)$, and $1(0)$ respectively at the $4f$, $4e$, $6g$, $12j$, $12j'$, and $12k$ sites. Hence, the Tm ions mainly occupy two crystallographic positions, $2b$ and $2d$, and the Fe atoms occupy four sites, $4f$, $6g$, $12j$, and $12k$. As noted above, Tm_b, Tm_d, Fe_f, Fe_g, Fe_j, and Fe_k denote the Tm and Fe ions that occupy these positions. Besides, there are additional $2c$ and $4e$ positions for the Tm and Fe ions; we use the notation Tm_c and Fe_e for them. The refined composition of the main phase is $Tm_{1.83}Fe_{17.34}$.

The neutron patterns collected below 288 K contain magnetic contributions to the intensities of nuclear reflections. With an HRPD diffractometer, we did not find any extra reflections associated with the long-range magnetic order in the range of the scanned angles $2\theta = 7°$–$159°$. Therefore, the wave vector is $\mathbf{k}_1 = 0$. At the same time, using a position-sensitive detector system, we found a broad maximum at $2\theta \approx 2.5°$ in the temperature interval 255–288 K (Fig. 2). This maximum may point to the existence of an incommen-

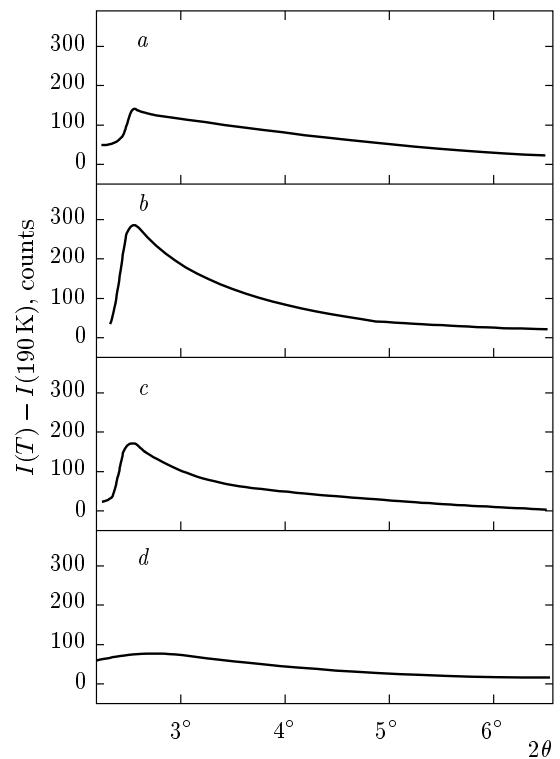surate magnetic structure with $\mathbf{k}_2 \approx (2\pi/c)(0, 0, 0.19)$. However, the width of the maximum is considerably larger than that of Bragg's reflections. This allows suggesting that the spin arrangement with $\mathbf{k}_2$ occurs only as a short-range magnetic order. In our sample, a long-range magnetic order with $\mathbf{k}_1 = 0$ realizes at temperatures below $T_C = 288$ K and it coexists with the short-range magnetic order in the temperature interval 255–288 K.

For $\mathbf{k}_1 = 0$, we performed a symmetry analysis of magnetic structures that are possible in a magnet with a disordered Th_2Ni_{17}-type crystal structure. For example, the decomposition of the magnetic representation for the $2b$ position is

$$2b : d_M = \tau_3 + \tau_6 + \tau_9 + \tau_{12}. \qquad (16)$$

The irreducible representations τ_i are numbered according to Kovalyov [21]. The basis functions of the irreducible representations entering the decomposition of the magnetic representations were calculated following Ref. [22]. They correspond to magnetic structures with the magnetic moments oriented along the c-axis or confined to the basal plane.

Table 1. Results of refinement for the nuclear and magnetic structures of $Tm_{1.83}Fe_{17.34}$. Notation: a and c are the lattice constants; x, y, and z are the coordinate parameters; μ_{Tm}^b and μ_{Tm}^d are the magnetizations of the thulium $2b$ and $2d$ sublattices; μ_{Fe}^f, μ_{Fe}^g, μ_{Fe}^j, and μ_{Fe}^k are the magnetizations of the iron $4f$, $6g$, $12j$, and $12k$ sublattices; R_{Br}^N, R_f^N, and R_{Mag} are the discrepancy factors for the crystal and magnetic structures

	10 K	80 K	100 K	140 K	200 K	300 K
a, Å	8.4182(1)	8.4169(1)	8.4164(1)	8.4185(1)	8.4213(1)	8.4230(1)
c, Å	8.3239(1)	8.3119(1)	8.3099(1)	8.3030(1)	8.2946(1)	8.2776(1)
z(Fe,$4e$)	0.112(2)	0.115(2)	0.112(2)	0.113(2)	0.116(2)	0.126(1)
z(Fe,$4f$)	0.1058(4)	0.1055(4)	0.1071(3)	0.1049(3)	0.1048(3)	0.1041(2)
x(Fe,$12j$)	0.3357(9)	0.3360(10)	0.3333(8)	0.3349(8)	0.3331(9)	0.3346(9)
y(Fe,$12j$)	0.3741(3)	0.3750(4)	0.3765(3)	0.3758(3)	0.3764(3)	0.3786(7)
x(Fe,$12j'$)	0.3100(11)	0.3056(11)	0.3106(10)	0.3073(9)	0.3068(10)	0.3075(9)
y(Fe,$12j'$)	0.3304(8)	0.3245(9)	0.3286(9)	0.3263(7)	0.3236(8)	0.3231(17)
x(Fe,$12k$)	0.1648(4)	0.1658(4)	0.1658(4)	0.1660(4)	0.1663(4)	0.1662(3)
z(Fe,$12k$)	0.9857(1)	0.9846(1)	0.9852(1)	0.9847(1)	0.9846(1)	0.9835(1)
μ_{Tm}^b (μ_B)	7.4(1)	6.1(1)	4.5(1)	3.4(1)	2.0(1)	—
μ_{Tm}^d, μ_B	6.9(1)	5.0(1)	4.5(1)	3.4(1)	2.0(1)	—
μ_{Fe}^f, μ_B	2.17(6)	2.06(8)	2.25(7)	2.03(7)	1.76(13)	—
μ_{Fe}^g, μ_B	1.42(7)	1.34(8)	1.40(10)	1.49(12)	1.21(22)	—
μ_{Fe}^j, μ_B	2.16(6)	2.15(8)	2.01(6)	1.80(6)	1.61(11)	—
μ_{Fe}^k, μ_B	1.60(5)	1.52(7)	1.69(6)	1.72(7)	1.47(13)	—
R_{Br}^N, %	6.7	7.5	5.3	6.2	6.1	6.2
R_f^N, %	6.7	7.5	5.3	6.2	6.1	6.2
R_{Mag}, %	7.6	10.0	11.4	12.3	12.9	—

To refine the crystallographic and magnetic structure parameters in the magnetically ordered state, the following constraints were set. The occupations numbers do not change with temperature at $T < 300$ K. The Tm_c and Tm_d ions have the same magnitudes and orientations of the magnetic moments. Taking into account that the $4e$- and $12j$-site average hyperfine fields exhibit similar behavior at the SRT [12], we also imposed the constraints on the Fe-atom moments at the $4e$, $12j$, and $12j'$ positions. As a result, only six (two thulium and four iron) sublattice magnetizations were determined; we use the notation μ_{Tm}^b, μ_{Tm}^d, μ_{Fe}^f, μ_{Fe}^g, μ_{Fe}^j, and μ_{Fe}^k for them.

A good agreement (see Fig. 3 and Table 1) between the observed and calculated intensities, resulting from various variants of mixing the basis functions, was obtained in the following cases. Below 75 K, the magnetic structure can be described by the τ_3 representation. The $\boldsymbol{\mu}_{Tm}^b$ and $\boldsymbol{\mu}_{Tm}^d$ magnetic moments are antiparallel to the $\boldsymbol{\mu}_{Fe}^f$, $\boldsymbol{\mu}_{Fe}^g$, $\boldsymbol{\mu}_{Fe}^j$, and $\boldsymbol{\mu}_{Fe}^k$ moments and are

oriented along the c-axis. At $T \geq 100$ K, the Tm- and Fe-moment arrangement can be described by the τ_9 representation. The obtained magnetic structure is also ferrimagnetic, but all the moments lie in the basal plane.

In the temperature range 75–100 K, an "easy axis–easy plane"-type SRT occurs. As can be seen from Fig. 3, the SRT is accompanied by a noticeable change in the intensity of some reflections on the powder diagrams; for instance, the intensity of the (100), (110), and (304) peaks decreases. However, the (002) peak, which is most appreciable for the study of the SRT, is not distinctly apparent on the powder diagrams because it is located close to the (110) peak. We therefore performed measurements of the (002) peak on a single crystal. The results are presented in the inset of Fig. 3. The magnetic contribution to the intensity of the (002) peak changes from zero to a maximal value as the Tb- and Fe-ion magnetic moments rotate from the c-axis to the basic plane. This occurs as the temperature in-
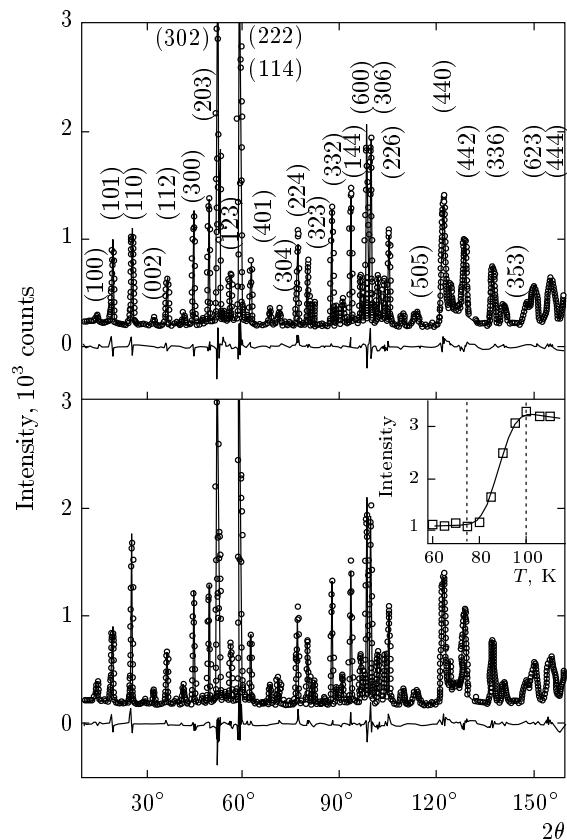
Fig. 3. The observed (points), calculated (solid lines), and difference (bottom lines) neutron diffraction profiles at (a) 105 K and (b) 75 K. Inset shows the temperature dependence of the integrated intensity of the (002) reflection, measured on a single crystal

creases from 75 to 100 K. In this temperature range, the magnetic structure can be considered, to within experimental accuracy, as a collinear ferrimagnetic one, and it is described as the sum of the τ_3 and τ_9 representations.

Using scans of the (002) peak and the powder diagrams, we obtained the experimental temperature dependence of the angle θ_{Tm} formed by the Tm-sublattice magnetizations with the c-axis. We supposed that this angle is the same for both Tm sublattices. The dependence is shown in Fig. 4. It can be seen that θ_{Tm} continuously changes from 0 to $\pi/2$ as the temperature increases. We determined the temperatures $T_{SR1} = 75$ K and $T_{SR2} = 100$ K.

Figure 5 presents the temperature dependences of the lattice parameters a and c and unit-cell volume V. We can see that the c parameter and the volume V decrease with increasing the temperature up to 300 K. The a parameter evidently decreases with temperature
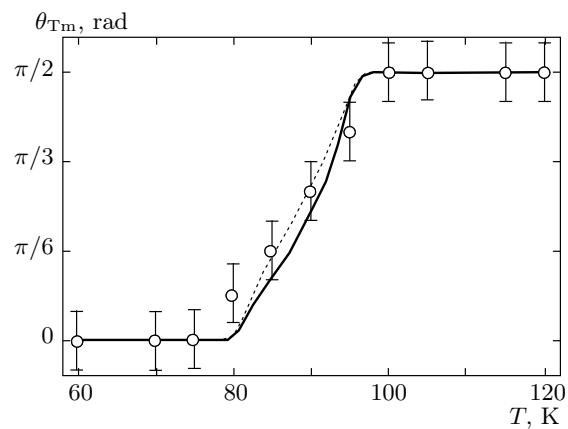

Fig. 4. Temperature dependence of the angle between the c axis and the Tm_b- and Tm_d-sublattice magnetizations. The points are experimental data, the solid line is the calculation for the Tm_b magnetization, and the dashed line is the calculation for Tm_d magnetization
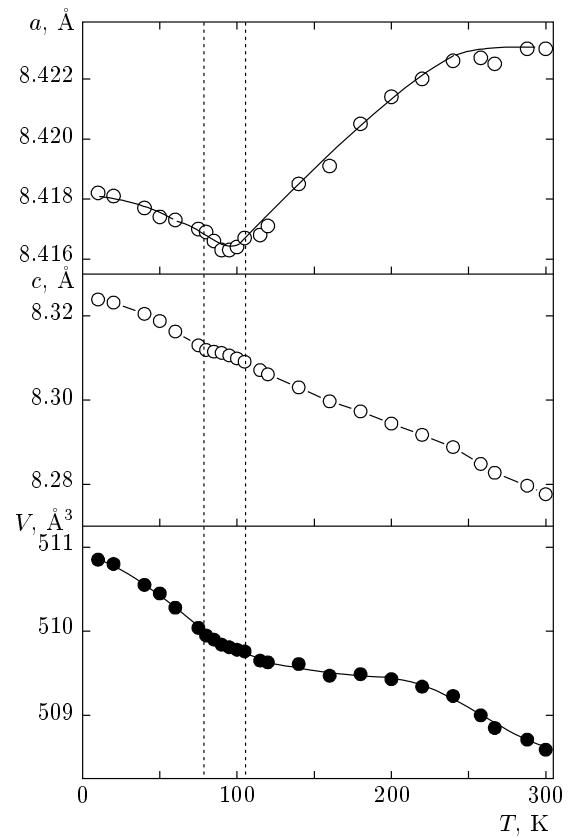

Fig. 5. Temperature dependences of the lattice parameters a and c and the unit-cell volume. The dashed lines indicate the beginning and end of the SRT
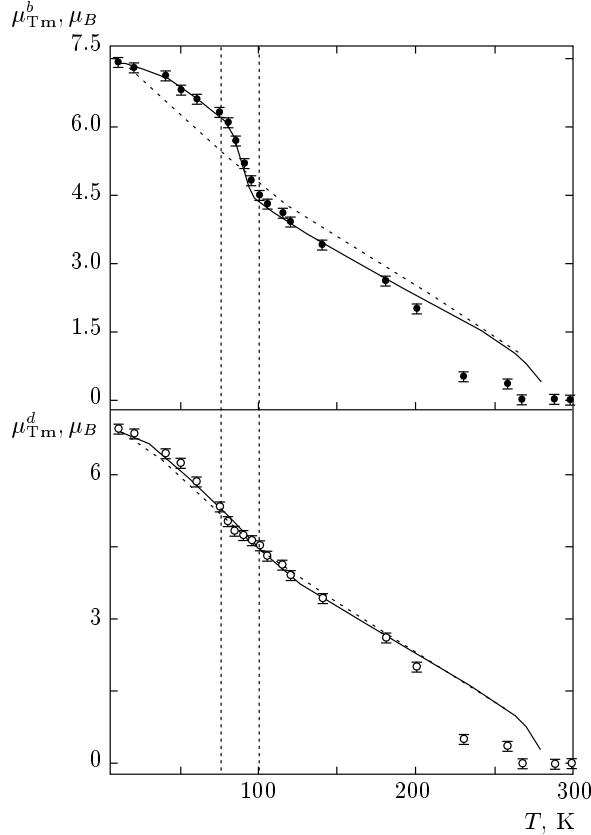
Fig. 6. Temperature dependence of the magnetization of the Tm sublattices; solid and light circles respectively stand for the Tm_b and Tm_d sublattices. The solid lines are calculations for $I = 235$ K/Tm-ion, $B_{20}^b = -1.2$ K, and $B_{20}^d = -0.3$ K. The dotted lines are computed for $I = 235$ K/Tm-ion and $B_{20}^b = B_{20}^d = 0$. The dashed lines indicate the beginning and end of the SRT

in the range 10–100 K, and it monotonically increases up to 250 K. Our dependences $a(T)$, $c(T)$, and $V(T)$ agree qualitatively with those obtained in Refs. [23, 24]. They show that an appreciable spontaneous magnetostriction exists in the $Tm_{1.83}Fe_{17.34}$ compound. The main contribution to the magnetostriction is caused by a change of the c-parameter even if the magnetic moments lie within the basal plane. It is interesting that the magnetostriction increases in the basal plane as the moments rotate to the c-axis.

Figure 6 shows the temperature dependences of the μ_{Tm}^b and μ_{Tm}^d magnetizations. The values of μ_{Tm}^b and μ_{Tm}^d are different below T_{SR1} and are the same above T_{SR2}. The curve $\mu_{Tm}^b(T)$ consists of three well-distinguished sections: the magnetization changes relatively weakly below T_{SR1} and above T_{SR2}, and the sharp change of μ_{Tm}^b corresponds to the temperature range

in which the SRT occurs. In this range, the $\boldsymbol{\mu}_{Tm}^b$ magnetization experiences a jump $\Delta\mu_{Tm}^b$. Assuming that in the SRT region, the dependence $\mu_{Tm}^b(T)$ is similar to that at $T > 100$ K, the value $\Delta\mu_{Tm}^b$ can be estimated as $1.2\mu_B$. Hence, the rotation of μ_{Tm}^b from the c-axis to the basal plane is accompanied by a relatively large change of the μ_{Tm}^b value. This points to the existence of a large magnetization anisotropy ($\Delta\mu_{Tm}^b/\mu_{Tm}^b \approx 20\%$) in the Tm_b sublattice.

In comparison with $\mu_{Tm}^b(T)$, the curve $\mu_{Tm}^d(T)$ is nearly monotonic. Nevertheless, there is some distinction in the character of the dependence $\mu_{Tm}^d(T)$ before and after the SRT. This originates from the magnetization anisotropy in the Tm_d sublattice. Our estimation results in the jump $\Delta\mu_{Tm}^d = (0.2–0.3)\mu_B$. Taking the occupation numbers into consideration, we obtain that the anisotropy of the Tm-subsystem magnetization is equal to $\Delta M_{Tm} \approx 1.2\mu_B$.

Figure 7 shows thermal variations of the Fe sublattice magnetizations. They reveal more or less observable changes of the magnetizations of all the sublattices in the SRT region. This is due to the magnetization anisotropy of the Fe atoms. Our data allow concluding that the magnetization anisotropy in the Fe_f, Fe_g, and Fe_k sublattices has the sign opposite to the one in the Fe_j sublattice. This agrees with the results obtained in Ref. [12] from Mössbauer measurements. From Fig. 7, we can estimate the values of the Fe-sublattice magnetization anisotropy as $\Delta\mu_{Fe}^f \approx 0.2\mu_B$, $\Delta\mu_{Fe}^g \approx 0.1\mu_B$, $\Delta\mu_{Fe}^j \approx -0.1\mu_B$, and $\Delta\mu_{Fe}^k \approx 0.1\mu_B$. Our results confirm the conclusions made in Refs. [12, 25, 26] that the Fe-atom magnetization anisotropy is most pronounced for the $4f$ position. The temperature dependence of the average magnetization of the Fe-subsystem is also given in Fig. 7. The curve $\mu_{Fe}^{av}(T)$ exhibits a slight anomaly in the SRT region, if any. The calculated value of $\Delta\mu_{Fe}^{av}$ is equal to $0.05\mu_B$.

Using the above magnitudes of the magnetization anisotropy in the Tm and Fe sublattices, we obtain that in the SRT region, the spontaneous magnetization anisotropy is equal to $1.9\mu_B$/f.u. This value agrees quite well with that determined in our magnetic measurement data (about $2\mu_B$/f.u.) [27].

5. DISCUSSION

According to Ref. [28], the Tm_2Fe_{17} compound has a simple spiral-type magnetic structure in the range 250–280 K and a collinear ferrimagnetic one below 250 K. We observed the $(000)^+$ magnetic satellite peculiar to a modulated magnetic structure. The angu-
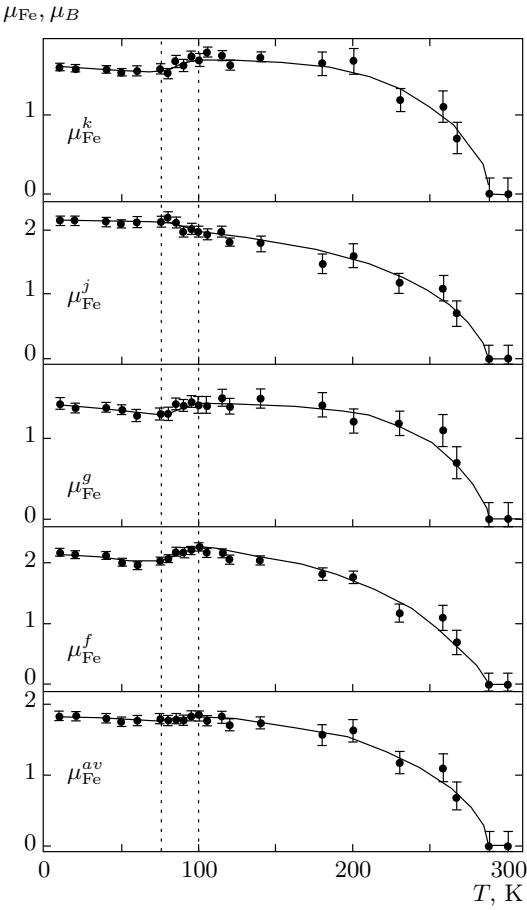
Fig. 7. Temperature dependences of the magnetization of the Fe_k, Fe_j, Fe_g, and Fe_f sublattices (μ_{Fe}^k, μ_{Fe}^j, μ_{Fe}^g, and μ_{Fe}^f) and the Fe susbsytem (μ_{Fe}^{av}). The dashed lines indicate the beginning and end of the SRT

lar position of the satellite points to the wave vector $\mathbf{k}_2 = (2\pi/c)(0, 0, 0.19)$. However, a relatively large half-width and the low intensity of the satellite allow assuming that there is only a short-range modulated magnetic order in our sample. The long-range magnetic order is realized as the ferrimagnetic structure with $\mathbf{k}_1 = 0$. A distinction in the magnetic states of our sample and that investigated in Ref. [28] can be related to their compositions. For the $\mathrm{R}_2\mathrm{Fe}_{17}$ compounds, the dependence of their magnetic properties on the composition becomes evident in a study of the $\mathrm{Ce}_2\mathrm{Fe}_{17}$ compound. A coexistence of the short-range modulated and long-range ($\mathbf{k} = 0$), ferromagnetic orders was found at low temperatures in [29]. On the other hand, a fan structure was detected in [30], whereas the exsistence of an antiferromagnetic phase is assumed in [31]. Obviously, a strong dependence of the magnetic state of the $\mathrm{R}_2\mathrm{Fe}_{17}$ sample on its composition is caused by

the presence of competitive (ferro- and antiferromagnetic) interactions between the Fe atoms at the different crystallographic positions. A relation between the ferro- and antiferromagnetic interactions changes with variation of the composition, which results in either a commensurate or an incommensurate magnetic structure.

In our sample, the long-range magnetic order can be described by the τ_3 or τ_9 irreducible representations with the orientations of magnetic moments being parallel or perpendicular to the c-axis. A feature of $\mathrm{Tm}_2\mathrm{Fe}_{17}$ (among the $\mathrm{R}_2\mathrm{Fe}_{17}$ compounds) is the existence of the magnetic structure (in the SRT range) described by the sum of the τ_3 and τ_9 representations. This means that the magnetic states (with spin configurations along the c-axis and in the basal plane) corresponding to the τ_3 and τ_9 representations have very close energy values in the SRT interval. These states form a single exchange multiplet. It can be split by anisotropic interactions. In the SRT interval, the MA energy is weak in comparison with the exchange energy; therefore, the splitting is small and the magnetic structure is described by the sum of the τ_3 and τ_9 representations appearing in a single multiplet. The anisotropy is evidently rather strong below T_{SR1} and above T_{SR2}, and hence the splitting of the exchange multiplet results in a difference of the energies of spin arrangements along the c-axis and in the plane.

To describe the $\mu_{\mathrm{Tm}}^b(T)$ and $\mu_{\mathrm{Tm}}^d(T)$ dependences, we use the equations in Sec. 3. The experimental data and the $\mu_{\mathrm{Tm}}^b(T)$ and $\mu_{\mathrm{Tm}}^d(T)$ curves calculated by means of Eqs. (5)–(8) are presented in Fig. 6. These curves are plotted for the parameter values $I = 23.2 \text{ MJ/m}^3$ (235 K/Tm-ion), $B_{20}^b = -1.2$ K, and $B_{20}^d = -0.3$ K. The value of I obtained by us is somewhat lower than the one ($I = 270$ K/Tm-ion) evaluated from Mössbauer measurements on $\mathrm{Tm}_2\mathrm{Fe}_{17}$ in Ref. [9]. At the same time, our B_{20}^b and B_{20}^d are noticeably different from $B_{20}^b = -0.5$ K and $B_{20}^d = 0.5$ K determined there. Our average value $B_{20} = -0.7$ K roughly agrees with $B_{20} = -0.4$ K found from the heat capacity measurements in Ref. [32].

Figure 6 also shows the $\mu_{\mathrm{Tm}}^b(T)$ and $\mu_{\mathrm{Tm}}^d(T)$ dependences calculated under the assumption that the B_{20}^b and B_{20}^d parameters are equal to zero. It can be easily seen (for $\mu_{\mathrm{Tm}}^b(T)$) that the experimental points spread above the curve with $B_{20}^b = 0$ at $T < T_{SR1}$ and below this curve at $T > T_{SR2}$. This is evidence of the fact that the MA has a strong effect on the temperature behavior of the μ_{Tm}^b magnetization. As mentioned above, the MA tends to keep individual magnetic moments aligned along the c-axis, which is the easy magnetiza-

tion direction for Tm ions. On the other hand, it enhances angular deviations between the moments when they lie in the basal plane (the hard magnetization direction for Tm ions). This results in the magnetization anisotropy $\Delta\mu_{Tm}^b$ in the SRT region. In the case of the μ_{Tm}^d magnetization, the difference between the experimental points and the curve calculated for $B_{20}^d = 0$ is inconsiderable. This points to a relatively low magnetization anisotropy of the Tm_d ions.

The information on B_{20}^b and B_{20}^d allows estimating the values of the MA constants for the Tm_b and Tm_d sublattices (K_{Tm}^b and K_{Tm}^d) by means of the well-known equitation [18]

$$K_1 = -3N_R B_{20} J \left(J - \frac{1}{2} \right), \qquad (17)$$

where N_R is the R-ion concentration. The constants K_{Tm}^b and K_{Tm}^d are presented in Table 2. As can be seen, they are positive and K_{Tm}^b is larger than K_{Tm}^d by about a factor of four. Our data qualitatively differ from the result obtained in Ref. [9], according to which the constants K_{Tm}^b and K_{Tm}^d have different signs ($K_{Tm}^b = 3.2$ MJ/m^3 and $K_{Tm}^d = -2.1$ MJ/m^3). If this were the case, the resulting MA constant of the Tm subsystem should be equal to 1.1 MJ/m^3. This value is smaller than K_{Fe}, but the opposite inequality, $K_{Tm} > K_{Fe}$ must be satisfied for the SRT to occur in Tm_2Fe_{17}.

Knowing the MA constants and the magnetizations of the Tm and Fe sublattices, we can evaluate the anisotropy field in our sample from the relation [18]

$$H_A = 2K_1/M_s, \qquad (18)$$

where M_s is the spontaneous magnetic moment. In our case, $K_1 = K_{Tm}^b + K_{Tm}^d - K_{Fe} = 66.2$ K/f.u., $M_s = M_{Fe} - M_{Tm} = 18.9\mu_B$/f.u., and the $\mu_0 H_A$ magnitude is then equal to 7 T. This value is rather close to 6 T, determined in magnetization measurements in [33]. On this ground, it could be expected that our value of K_{Tm} would agree quite well with that obtained from the magnetization curves ($K_{Tm} = 6.7$ MJ/m^3 [34]).

As mentioned above, the R-ion magnetization anisotropy originates from the MA energy, which exerts a strong influence on the population of the low-energy levels of an R ion at finite temperatures. When the magnetic moments are oriented along the easy magnetization direction, the distances between low-energy levels become larger than in a scheme ignoring the MA. On the other hand, if the moments are oriented along the hard magnetization direction, these distances are shorter than those for zero magnetic anisotropy.
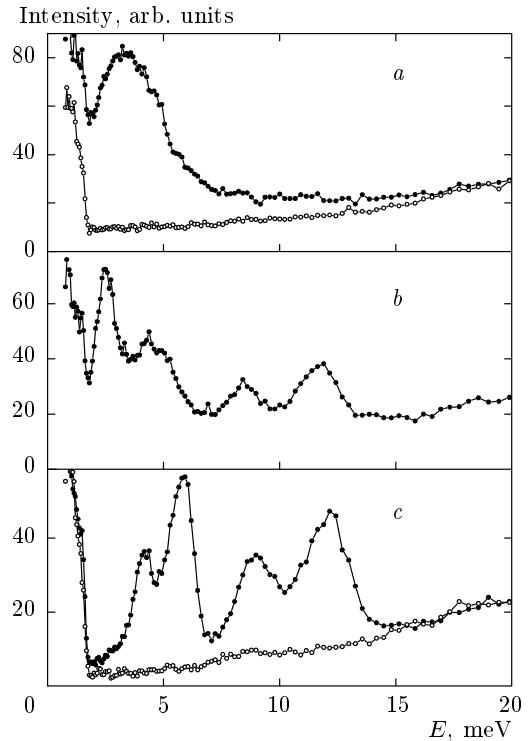

Fig. 8. Inelastic neutron scattering spectra of $Tm_{1.83}Fe_{17.34}$ (solid points) and Y_2Fe_{17} (light points) at (*a*) 120 K, (*b*) 60 K, and (*c*) 10 K

Then the population of the low-energy levels must be higher in the former case than in the latter. Therefore, we can suppose that the R-ion energy scheme should change under the SRT. To verify this assumption, we performed inelastic neutron scattering (INS) measurements.

Figure 8 shows the low-energy part of the INS spectrum for $Tm_{1.83}Fe_{17.34}$ at temperatures below (10 and 60 K) and above (120 K) the SRT region. To determine the background due to Fe–Fe dispersive modes and phonon scattering, we also performed the INS experiment on Y_2Fe_{17}. The INS spectra for Y_2Fe_{17} are also shown in Fig. 8. It is seen that the INS spectrum of $Tm_{1.83}Fe_{17.34}$ obtained at 10 K contains four peaks at about 4.2, 5.8, 9.0, and 12.1 meV. Their intensities change slightly with temperature up to 60 K and the line at 2.4 meV appears. As the temperature increases to 120 K (and magnetic moments rotate from the *c*-axis to the basal plane), the INS spectrum evidently changes. Only one sharp peak around 3.5 meV can be seen in the spectrum. Hence, the SRT results in a significant change of the INS spectrum. It is worth noting that such a strong change of the INS spectrum was not previously observed in R–T compounds under

the SRT, although the INS measurements were carried out on a series of R–T systems (for example, the SRT in $Nd_2Fe_{14}B$ [35]).

A calculation of the INS spectrum will be performed in the future. Presently, we can only make a rough estimate. The Tm-ion moments are oriented along their own easy axis at 10 K and transitions from the ground state to the first excited level are possible. Therefore, two peaks caused by two Tm-site types should be observed in the INS spectrum. The presence of two additional peaks could be explained by a difference in the surroundings of the Tm_b and Tm_d ions due to Fe atoms in the $4e$ position. The ratio between the total intensity of the first pair of the peaks and that of the second pair is $0.74 : 1.0$. This is well in accord with $0.76 : 1.0$, which corresponds to the ratio of the occupation numbers for the Tm_b and Tm_d ions. We can therefore conclude that the first pair of peaks originates from the Tm_b ions and the second pair relates to the Tm_d ones.

All the CEF parameters are impotant for the calculation of the INS spectrum. The information on B_{20} allows only estimating an order of the energy of the transition from the level $|J\rangle$ to the nearest one, $|J-1\rangle$. The energy difference between these levels is

$$\Delta E = [-I_{RT}(J-1) + 3B_{20}(J-1)^2] -$$
$$- [-I_{RT}J + 3B_{20}J^2] = I_{RT} - 3(2J-1)B_{20}. \quad (19)$$

The substitution of the values of I_{RT} and B_{20}^b in this equation leads to the value $\Delta E = 6.8$ meV. This rather well agrees with the energy of the first pair of the peaks.

We now consider the MA of the Fe sublattices in $Tm_{1.83}Fe_{17.34}$. As shown in Sec. 3, in order to estimate the Fe sublattice MA constants, we can apply the model of the MA of a system with an incompletely quenched orbital magnetic moment [13]. According to this model, the MA of the Fe atoms is proportional to the Fe-atom magnetization anisotropy.

Using Eqs. (14) and (15), the occupation numbers, the magnitudes of the Fe sublattice magnetization anisotropy obtained by us, and the value of K_{Fe} taken from Ref. [16], we estimated the Fe sublattice MA constants, which are given in Table 2. According to our estimation, the in-plane anisotropy of the Fe subsystem is due to the Fe atoms in the $4f$, $6g$, and $12k$ positions. On the contrary, the Fe_e and Fe_j sublattices exhibit a uniaxial anisotropy. The largest MA (calculated per Fe atom) is found in the Fe_f sublattice. Our result regarding the different MA types of the Fe sublattices agrees qualitatively with that obtained for the rhombohedral $Y_2(Co,Fe)_{17}$ compounds in Ref. [36], where the sublattice MA constants were evaluated in terms

Table 2. The magnetic anisotropy constants of the Tm and Fe sublattices in $Tm_{1.83}Fe_{17.3}$. Notation: Tm_b, Tm_c, and Tm_d are the thulium $2b$, $2c$, and $2d$ sublattices; Tm_{tot} is the Tm subsystem; Fe_e, Fe_f, Fe_g, Fe_j, and Fe_k are the iron $4e$, $4f$, $6g$, $12j$, and $12k$ sublattices; Fe_{tot} is the Fe subsystem

Sublattice	K, MJ/m³,	K, K/ion
Tm_b	5.0	119
Tm_c	0.1	30
Tm_d	1.6	30
Tm_{tot}	6.7	72
Fe_e	0.2	9
Fe_f	−1.9	−18
Fe_g	−1.4	−9
Fe_j	2.9	9
Fe_k	−2.9	−9
Fe_{tot}	−3.1	−58 [17]

of a combination of the experimental bulk anisotropy and neutron diffraction data on the preferential occupation of the Co and Fe atoms of the crystallographic positions.

In the framework of the MA model of a system with an incompletely quenched orbital magnetic moment, we can also estimate the parameter of the spin–orbital coupling in Eq. (13). The substitution of $K_{Fe}^f = 18$ K/Fe-at., $\Delta\mu_{Fe}^f = 0.2\mu_B$, and $S = 1$ in Eq. (13) leads to $\lambda = 180$ K. Our value of λ is quite close to that (about 300 K) obtained for the $3d$ transition metals [18]. This allows suggesting that the MA model of the system with an incompletely quenched orbital magnetic moment gives, at least, a true order of magnitude of the Fe sublattice MA constants.

6. SUMMARY

The $Tm_{1.83}Fe_{17.34}$ compound was investigated by means of neutron diffraction and INS. The compound crystallizes in a partially disordered Th_2Ni_{17}-type structure. The long-range ferrimagnetic order with $\mathbf{k}_1 = 0$ exists up to $T_C = 288$ K. This order coexists with the short-range magnetic one ($\mathbf{k}_2 \approx (2\pi/c)(0,0,0.19)$) in the temperature range 255–288 K. Upon increasing the temperature, the compound undergoes the SRT from the c-axis to the basal plane at $T_{SR1} = 75$ K and $T_{SR2} = 100$ K.

The temperature dependences of two Tm- and four Fe sublattice magnetizations in $Tm_{1.83}Fe_{17.34}$ have been determined. All the dependences point to existence of magnetization anisotropy in the temperature range where the SRT occurs. The largest magnetization anisotropy ($1.2\mu_B$/Tm-ion) was observed in the Tm sublattice formed by the Tm ions at the $2b$ position.

The two-subsystem model of the MA was modified. The magnitude and orientation of the Tm-subsystem magnetization is calculated at a given temperature by minimization of the anisotropy energy with a single varying parameter, which is the angle between the c-axis and the Fe subsystem magnetization. We applied this model for the evaluation of the values of the Tm–Fe exchange parameter and the CEF parameters B_{20}^b and B_{20}^d for two Tm positions. The anisotropy constant of the Tm ions at the $2b$ position is by a factor of four higher than that at the $2d$ site. The MA energy of the Tm_b sublattice is only by a factor of five lower than the Tm–Fe exchange energy. This causes the large magnetization anisotropy of the Tm ions at the $2b$ position.

To estimate the MA constants of the Fe sublattices, the model of the MA of a system with an incompletely quenched orbital magnetic moment was applied. It was obtained within the model that the Fe sublattice MA constants are proportional to the Fe-atom magnetization anisotropy determined in the SRT region. The large in-plane anisotropy of the Fe subsystem is caused by Fe atoms at the $4f$, $6g$, and $12k$ positions, while Fe atoms at the $12j$ position favor the uniaxial anisotropy. We revealed that the INS spectra of $Tm_{1.83}Fe_{17.34}$ change noticeably under the SRT.

REFERENCES

1. R. Skomski and D. J. Sellmyer, J. Rare Earths **27**, 675 (2009).

2. A. S. Ermolenko, E. V. Rosenfeld, Yu. N. Irkhin et al., Zh. Eksp. Teor. Fiz. **69**, 1743 (1975).

3. N. H. Luong, Physica B **319**, 90 (2002).

4. M. T. Hutchings, Sol. St. Phys. **16**, 227 (1964).

5. N. Plugaru, J. Rubin, J. Bartolome et al., Phys. Rev. B **65**, 134419 (2002).

6. M.-H. Yu and Z.-D. Zhang, J. Magn. Magn. Mater **232**, 60 (2001).

7. O. Tegus, E. Bruck, A. A. Menovsky et al., J. Alloys Comp. **302**, 21 (2000).

8. O. Bardyn, B. Belan, R. Gladyshewskii et al., Chem. Met. Alloys **3**, 69 (2010).

9. P. C. M. Gubbens, A. M. Kraan, J. J. Loef, and K. H. J. Buschow, J. Magn. Magn. Mater. **67**, 255 (1987).

10. V. Yu. Irkhin and Yu. P. Irkhin, Phys. Rev. B **57**, 2697 (1998).

11. Yu. P. Irkhin and V. Yu. Irkhin, Phys. Sol. St. **43**, 274 (2001).

12. F. Grandjean, O. Isnard, and G. J. Long, Phys. Rev. B **65**, 064429 (2002).

13. E. V. Rosenfeld and A. V. Korolev, Zh. Eksp. Teor. Fiz. **108**, 862 (1995).

14. J. Rodriguez-Carvajal, Physica B **192**, 55 (1993).

15. E. R. Callen and H. B. Callen, J. Phys. Chem. Sol. **16**, 310 (1960).

16. B. Matthaei, J. J. M. Franse, S. Sinema, and R. J. Radwanski, J. de Phys. **49**, C8-533 (1988).

17. A. V. Andreev, D. Rafaja, J. Kamarad et al., Physica B **348**, 141 (2004).

18. K. H. J. Buschow, *Handbook of Magnetic Materials*, Vol. 10, ed. by K. H. J. Buschow, North Holland, Amsterdam (1997), p. 463.

19. P. Larson and I. I. Mazin, J. Magn. Magn. Mater. **264**, 7 (2003).

20. O. Moze, R. Caciuffo, B. Gillon et al., Phys. Rev. **50**, 9293 (1994).

21. O. V. Kovalev, *Representation of the Crystallographic Space Groups: Irreducible Representations, Induced Representations and Corepresentations*, ed. by H. T. Stokes and D. M. Hatch, Gordon and Breach Sci. Publ., Amsterdam (1993), p. 349.

22. Yu. A. Izyumov, R. P. Ozerov, and V. E. Naish, *Neutron Diffraction of Magnetic Materials*, Consultant Bureau, Plenum Publ. Corp., New York (1991), p. 82.

23. A. V. Andreev, *Handbook of Magnetic Materials*, Vol. 8, ed. by K. H. J. Buscow, North Holland, Amsterdam (1995), p. 59.

24. Y. Hao, X. Zhang, B. Wang et al., J. Appl. Phys. **108**, 023915 (2010).

25. M. T. Averbuch-Pouchot, R. Chevalier, J. Deportes et al., J. Magn. Magn. Mater. **68**, 190 (1987).

26. P. C. M. Gubbens, A. M. van der Kraan, T. H. Jacobs, and K. H. J. Buschow, J. Magn. Magn. Mater. **80**, 265 (1989).

27. J. Park, Y. Jo, J.-G. Park et al., J. Magn. Magn. Mater. **237**, 158 (2001).

28. D. Givord and R. Lemaire, in *Proceedings ICM-73*, Vol. III, Nauka, Moscow (1974), p. 492.

29. O. Prokhnenko, C. Ritter, Z. Arnold et al., J. Appl. Phys. **92**, 385 (2002).

30. D. Givord and R. Lemaire, IEEE Trans. Magn. **10**, 109 (1974).

31. Y. Janssen, H. Fujii, T. Ekino et al., Phys. Rev. B **56**, 13716 (1997).

32. C. Pique, R. Burriel, D. Fruchan et al., IEEE Trans. Magn. **30**, 604 (1994).

33. X. C. Kou, F. R. de Boer, R. Grössinger et al., J. Magn. Magn. Mater. **177–181**, 1002 (1998).

34. A. V. Andreev, A. V. Deryagin, S. M. Zadvorkin et al., *Physics of Magnetic Materials*, ed. by D. D. Nishin, Kalinin University, Kalinin (1985), p. 26. (in Russian).

35. H. Mayer, M. Steiner, N. Stusser et al., J. Magn. Magn. Mater **97**, 210 (1991).

36. T. P. Thuy and J. J. M. France, J. Magn. Magn. Mater. **54–57**, 915 (1986).